

# Emergence of non-Fickian transport in truncated pluri-Gaussian permeability fields

Eugenio Pescimoro<sup>1\*</sup>, Matteo Icardi<sup>1</sup>, Giovanni Porta<sup>2</sup>  
and Marco Bianchi<sup>3</sup>

<sup>1\*</sup>Industrial and Applied Mathematics, University of  
Nottingham, University Park, Nottingham, NG7 2RD,  
Nottinghamshire United Kingdom.

<sup>2</sup>Civil and Environmental Engineering, Politecnico di Milano,  
Piazza L. Da Vinci, 32, Milan, 20133, Lombardia, Italy.

<sup>3</sup>British Geological Survey, Nicker Hill, Keyworth, NG12 5GG,  
Nottinghamshire, United Kingdom.

\*Corresponding author(s). E-mail(s):

[eugenio.pescimoro@gmail.com](mailto:eugenio.pescimoro@gmail.com);

Contributing authors: [matteo.icardi@nottingham.ac.uk](mailto:matteo.icardi@nottingham.ac.uk);

[giovanni.porta@polimi.it](mailto:giovanni.porta@polimi.it); [marcob@bgs.ac.uk](mailto:marcob@bgs.ac.uk);

## Abstract

We present a numerical simulation study of advective-diffusive scalar transport in three-dimensional high-contrast discontinuous permeability fields, generated with a truncated pluri-Gaussian geostatistical approach. A range of permeability contrasts, correlation lengths, and Péclet numbers are studied to characterise the transition to non-Fickian transport behaviour. This is triggered by high permeability contrasts between different zones and is enhanced by the presence of connected higher permeability channels, which are characterised by high advective flow velocities. In this case, the overall transport behaviour deviate from the macroscopic advection-dispersion model based on a Fickian analogy. The numerical experiments are run with an Eulerian approach using a novel unified numerical framework based on the finite-volume library OPENFOAM<sup>®</sup>, for i) generating random pluri-Gaussian porous media, ii) solving the steady state Darcy-scale flow, iii) solving the advection diffusion equation, iv) computing post-processing quantities such as first order statistics, spatial probability density functions and

breakthrough curves. We identify a hierarchy of non-Fickian transport triggering factors, the strength of permeability contrast being the pivotal driver. The Péclet number and the characteristic length at which facies transitions are observed as secondary factors. Transport remains Fickian when the facies conductivities differ by up to one order of magnitude. Greater permeability contrasts act strengthen the emergence of fast flow channels leading to non-Fickian transport.

**Keywords:** Heterogeneous media, pluri-Gaussian simulations, Solute transport, OpenFoam, non-Fickian transport

## 1 Introduction

Subsurface flow and solute transport modelling is used in several engineering and environmental fields (CO<sub>2</sub> storage, groundwater remediation, oil recovery) where mathematical and computational models play a central role in supporting the reliability of analysis and design strategies. The effectiveness of advection-dispersion models in describing solute transport in highly heterogeneous media such as geological formations has been questioned [1–3], and the definition of appropriate models and their parameterization remains an open field of research [4–6]. An important challenge is how to simulate non-Fickian behaviour, which originates mainly from physical heterogeneities emerging across multiple scales [7, 8]. Transport is defined as anomalous or non-Fickian when solute plumes and breakthrough curves display a significant departure from the predictions made by an advective-dispersive model where dispersion is expressed with a Fickian analogy, i.e. is lumped with molecular diffusion in a single effective coefficient [9].

Approaches to modelling solute transport in heterogeneous porous media largely differ depending on the scale of interest. In this work we start from a mesoscale, which corresponds to a resolution where geological media can be described by an equivalent continuum with spatially heterogeneous properties [10, 11]. At this scale, solute transport is governed by two separate mechanisms: advection and local hydraulic dispersion which includes the contributions of molecular diffusion and mechanical dispersion. At the mesoscale, spatial heterogeneity is explicitly modelled, most commonly using a statistical characterization. We then move to macroscale modelling, where the aim is to define an effective model able to describe the dynamics of the system without an explicit description of the underlying heterogeneity. In classical descriptions [12], velocity at these scales may be interpreted as the average Darcy velocity while the hydraulic dispersion coefficient turns into a macrodispersion coefficient, employed to quantify the effect of heterogeneity on solute spreading. This model has been questioned in the literature and alternative non-Fickian effective models have been proposed [13–15]. These approaches mainly focused on cases where the underlying (mesoscale) log-conductivity

field has a Gaussian distribution. Beyond this specific case, the validity of the Advection Dispersion Equation (ADE) based macrodispersive models are not clearly identifiable a priori, although they are certainly heavily controlled by the degree of heterogeneity of porous media properties and their spatial organisation [15]. Discontinuous permeability fields with a high connectivity degree and sharp contrast between regions are recognised among the most important factors that regulate the transport of solute [16]. Aquifers characterized by highly connected *facies*, i.e. finite portion of the subsurface with similar physical properties, and high permeability contrasts are characterised by fast flow channels with persistent spatial velocity correlations, which make the overall solute behaviour non-Fickian [6]. The persistence of this anomalous transport behaviour at the macroscale can be due, for example, to these regions where the flow paths create preferential fast channels [17], a feature that also influences reactive transport settings [18, 19].

In this work we investigate solute transport and the onset of anomalous or non-Fickian transport behaviour in high-contrast heterogeneous permeability fields, generated with the geostatistical pluri-Gaussian truncated (PGS) method [20]. Solute transport has been widely investigated in continuous Gaussian and non-Gaussian permeability fields [21, 22], and methods have also been proposed to handle non-continuous fields, suitable to reproduce geomaterials where property transition is marked by sharp interfaces [23]. PGS random fields are used in this context to model actual subsurface geological media in a sedimentary setting. In this context this model is used to link an assumed geological architecture or structure, e.g. driven by sedimentological rules, with the spatial distribution of physical properties such as porosity or hydraulic conductivity. This allows to create fields starting from given geological assumptions and explicitly control the connectivity of high- and low-permeability facies. Therefore, PGS can be employed to reproduce and interpret the emergence of non-Fickian transport traits observed in real geological media. However, to our knowledge, studies that systematically address the impact of PGS field parameterization with solute transport features are lacking. Our aim here is to fill this gap and investigate the connectivity and permeability contrast thresholds that drive a transition between Fickian and non-Fickian. We quantify the deviation of the results obtained from numerical simulations in PGS domains from Fickian behavior by comparing them to the analytical solution of the advection-dispersion equation. This allows us to identify the physical and structural characteristics of the geological media that can lead to non Fickian transport and ultimately paves the way towards aquifer typing approaches where non Fickian transport features may become identifiable from a knowledge of the properties of the field.

To achieve these objectives we rely on numerical transport simulations, by solving the advection-dispersion equation in heterogeneous media using an Eulerian finite volume method. This approach is implemented as a parallel open-source code based on OPENFOAM<sup>®</sup>, as part of the SECUREFoam library [24]. The advantages of the Eulerian approach are that it allows the

computation of Péclet number and that an accurate simulation of solute low concentration tails does not require a large particle ensemble as with Lagrangian formulations, which have often been used in the recent literature [7, 17, 25]. Moreover, the Eulerian description is closer to the experimental conditions where results are often obtained in terms of molar or mass concentration while Lagrangian approaches need to be postprocessed to obtain local concentration fields.

From an operational perspective, our approach is based on a single computational framework, including a geostatistical algorithm for permeability field generation, a numerical code for flow and transport simulation, and post-processing tools. This is an interesting feature of our approach as the synthetic generation of realistic geological domains remains one of the main challenges in modelling flow and transport [26]. Several approaches are available to reproduce complex subsurface structures (sequential Gaussian simulations [27], Markov chain probability [28], Multiple-point statistics [29]) as well as a number of geostatistical open toolboxes (GSLib [30], T-PROGS [31]). Nevertheless, few tools exist that provide integrated geostatistical, flow and transport simulation solvers (OpenGeoSys [32], porousMultiphaseFoam [33], DuMux [34]).

This work is structured as follows: in Section 2 we give the mathematical overview of the problem, in Section 3 we describe the testcases and summarise the numerical methodologies. Numerical results and the post-processing are presented in Section 4, before we draw conclusions and give some guidelines about the emergence of non-Fickian transport. For the sake of clarity, the terms “facies” (uncountable) and “category” as well as “lithotype” and “truncation” rule will be used interchangeably depending on the context.

## 2 Methods

We describe here the methods underpinning our numerical simulations. We start by presenting the geostatistical framework and then move to the description of the physical problem, i.e. the flow and transport setting.

### 2.1 Geostatistical model

The permeability fields used in this work are generated via the pluri-Gaussian Simulation (PGS) method, i.e. applying a truncation rule to continuous multivariate Gaussian random fields (GRF) [20]. Fields generated with this approach are characterised by:

- discontinuous permeability fields characterised by a discrete number of zones of uniform permeability whose spatial arrangement is the result of a specific truncation rule (i.e. Lithotype rule [35]);
- high geological realism since the truncation rule allows to simulate observed geometrical relations between geological facies [35–37].

GRFs can be generated in the frequency domain by multiplying independent complex Gaussian random variables by the spectral representation of the covariance function. The spatial field is then reconstructed by applying the inverse Fourier transform to the spectral GRF. To ensure independence of the random field generation from the mesh-discretisation and to allow arbitrary unstructured grids, we apply an explicit discrete inverse Fourier transform discretised with  $N_f$  frequencies in each direction instead of the IFFT algorithm. Following [26, 38], a discrete-in-frequencies, continuous-in-space representation of a complex GRF is therefore given by:

$$Z(\mathbf{x}) = \sum_{j=0}^{N_f} \cos(2\pi \mathbf{a}_j \cdot \mathbf{x}) \sqrt{S(\mathbf{a}_j)} W_j + i \sum_{j=0}^{N_f} \sin(2\pi \mathbf{a}_j \cdot \mathbf{x}) \sqrt{S(\mathbf{a}_j)} W'_j \quad (1)$$

where  $\mathbf{x}$  is the position vector,  $\mathbf{a}_j = (a_{x,j}, a_{y,j}, a_{z,j})$  is the  $j^{th}$  frequency vector,  $W_j$  and  $W'_j$  are independent complex Gaussian random variable and  $S(\mathbf{a}_j)$  is the amplitude of the spectral measure. From  $Z$ , we can then extract two independent Gaussian random fields from its real and imaginary parts and compute it on an arbitrary spatial discretisation.

The covariance function of a stationary field quantifies the covariance  $\gamma(\mathbf{r})$  between a pair of values of a random variable located at points separated by the distance  $\mathbf{r}$ . The correlation function  $\rho(\mathbf{r})$  is the covariance function scaled by the variance  $\sigma^2$ , i.e.,  $\gamma(\mathbf{r}) = \sigma^2 \rho(\mathbf{r})$ .

In this work, we assume an exponential correlation function

$$\rho(\mathbf{r}) = 1 - e^{-\sqrt{\frac{r_x^2}{\lambda_x^2} + \frac{r_y^2}{\lambda_y^2} + \frac{r_z^2}{\lambda_z^2}}} \quad (2)$$

and corresponding spectrum

$$S(\mathbf{a}) = \sigma^2 \|\boldsymbol{\lambda}\|^d \frac{\Gamma\left(\frac{d+1}{2}\right)}{\left(\pi \left(1 + a_x^2 \lambda_x^2 + a_y^2 \lambda_y^2 + a_z^2 \lambda_z^2\right)\right)^{\frac{d+1}{2}}}, \quad (3)$$

where  $d = 3$  is the number of dimensions,  $\Gamma$  is the Gamma function,  $\boldsymbol{\lambda} = (\lambda_x, \lambda_y, \lambda_z)$  are the correlation lengths.

GRFs are continuous fields, but geological media are often characterised by abrupt changes in physical and chemical properties. With the PGS approach discontinuous patterns are reproduced from the truncation of two GRFs according to a *lithotype* or *truncation rule* (fig. 1), which bins continuous values into a set of categories. The smooth transition which characterizes the GRF is then replaced by  $n = (N_r + 1)(N_s + 1)$  categorical values where  $N_r$  and  $N_s$  are the number of thresholds applied via the truncation rule to the two GRFs. In this sense, the “truncated” adjective refers to a GRF that has been discretized through a binning process. The probability, i.e. the proportion, of

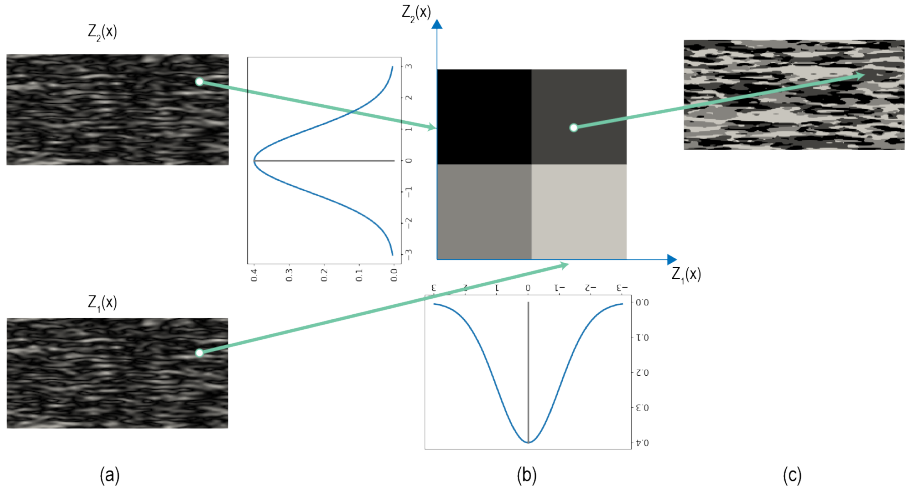


**Fig. 1** Truncated pluri-Gaussian simulation. a) Continuous multivariate Gaussian random fields  $Z_1$  and  $Z_2$  generation; b) truncation rule for four facies domain and its corresponding thresholds on the Gaussian distribution of the variables; c) sample of a two-dimensional truncated pluri-Gaussian random field. The arrows indicate the contribution of the two GRFs in assigning a given category at a selected location in space.

the facies  $\varphi_i$  is obtained from

$$p_{\varphi_i}(\mathbf{x}) = [G(r_i) - G(r_{i-1})][G(s_i) - G(s_{i-1})] \quad i = 1 \dots n \quad (4)$$

where  $n$  is the number of categories,  $G$  is the cumulative Gaussian distribution with the mean and the variance typical of each field. The lithotype rule allows to control the chances of a certain category of being into contact with the others. This constitutes a fundamental feature as it allows the simulated field to reflect geological transition patterns observed in field data. Typically, transition patterns are captured along the vertical direction by processing field sample information through transition probability matrices [39, 40] while field observations and/or established conceptual models of geological environments are used as guidance for the estimation of transition patterns in the horizontal directions [35]. In this work, we assume the single truncation diagram, in Fig. 1, while changing the correlation lengths  $\lambda$  of the underlying GRFs and the permeability values assigned to different categories. These four categories have also equal probability and therefore volumetric fractions  $p_{\varphi_i} = 25\%$ . The distribution of the multivariate random variables adopted to generate the underlying continuous Gaussian random fields in this study has mean  $\mu = 0$  and  $\sigma = 1$  and their correlation function is exponential with different values of correlation length.

## 2.2 The flow model

We assume fluid flow obeys the standard Darcy's equation which reads

$$\mathbf{V} = -\frac{\mathbf{k}}{\mu}(\nabla p + \rho g \nabla z), \quad (5)$$

where  $\mathbf{V}$  is the Darcy velocity vector [ $LT^{-1}$ ],  $\mathbf{k}$  is the permeability tensor [ $L^2$ ],  $\mu$  is the dynamic viscosity [ $ML^{-1}T^{-1}$ ],  $p$  is the pressure [ $MT^{-2}L^{-1}$ ],  $\rho$  is the fluid density [ $ML^{-3}$ ],  $g$  is the gravity constant [ $LT^{-2}$ ] and  $\nabla z = (0, 0, 1)$  [ $-$ ] is an upward unit vector. For this study we set  $g = 0$  as any influence of the solute on the liquid density is assumed to be negligible.

The flow solver implemented in OPENFOAM<sup>®</sup> is based on equation (5) assuming an incompressible fluid. Therefore pressure can be computed according to a Poisson equation

$$\nabla \cdot \mathbf{V} = -\nabla \cdot \frac{\mathbf{k}}{\mu} \nabla p = 0 \quad (6)$$

where we have assumed no sources or sinks are present and the gravity term is zero. The permeability tensor is, from this point, assumed diagonal and isotropic, i.e.,  $\mathbf{k} = k\mathbb{I}$ ,  $\mathbb{I}$  being the identity matrix.

## 2.3 Local transport model

The advective flux per unit area  $\mathbf{J}_{adv}$  [ $LT^{-1}$ ] is the product of the advective Darcy velocity  $\mathbf{V}$  [ $LT^{-1}$ ] and solute concentration  $c$  [ $-$ ]

$$\mathbf{J}_{adv} = \mathbf{V}c. \quad (7)$$

In line with previous work [17], we neglect mechanical dispersion and model the diffusive fluxes  $\mathbf{J}_{mol}$  [ $LT^{-1}$ ] as

$$\mathbf{J}_{mol} = -\phi \mathbf{D}_{mol} \nabla c \quad (8)$$

where  $\mathbf{D}_{mol}$  [ $L^2T^{-1}$ ] is the molecular diffusion tensor and  $\phi$  is the porosity of the medium. Summing up the advective and diffusive fluxes, the conservation of mass yields the advection-diffusion equation, which, for the case of isotropic diffusion and porosity and no source/sink terms is

$$\frac{\partial c}{\partial t} + \nabla \cdot (\mathbf{v}c) - \mathbf{D}_{mol} \nabla^2 c = 0 \quad (9)$$

where  $\mathbf{v} \equiv \mathbf{V}/\phi$  is the fluid velocity, i.e. the velocity that would be measured by a flow meter in the porous domain and  $\mathbf{D}_{mol} = D\mathbb{I}$ . The concentration boundary conditions adopted to solve (9) are fixed single concentration on the inlet, no flux on all lateral sides and zero gradient on the outlet of the domain.

In this study, to focus on the effects of the heterogeneity, the geostatistical parameters and the Péclet number, we have made strong assumptions on the permeability (isotropic and diagonal), porosity (constant) and neglected mesoscopic dispersion. Whilst preliminary tests suggested these do not impact the main findings of this work, the investigation of these processes may be tackled in future contributions.

## 2.4 Macrodispersion model

Transport mechanisms described so far characterise the transport behaviour at the mesoscale, i.e. where geological and flow resolution allows for heterogeneity to be modelled explicitly. However, macroscale models aim to provide an overall description while using an effective/upscaled advection-dispersion equation neglecting heterogeneity. Here, we only focus on transport along the main velocity direction and the longitudinal dispersion processes, therefore we will compare our results with a one-dimensional advection-dispersion equation:

$$\frac{\partial C}{\partial t} + \bar{v}_x \frac{\partial C}{\partial x} - D_{xx}^{mac} \frac{\partial^2 C}{\partial x^2} = 0, \quad (10)$$

where  $C$  is the section-averaged concentration and the longitudinal component of the macrodispersion tensor is  $D_{xx}^{mac}$ . The  $\bar{X}$  notation indicates the spatial average of the field  $X$  at a given section, also known as section average. Macrodispersion in Fickian transport models is often represented as the product between a typical length scale and an average velocity (13).

## 2.5 Quantities of interest

The record of the section-averaged concentration in time at a control section (e.g. outlet boundary or an arbitrary point) constitutes the breakthrough curve (BTC). Under a continuous injection, the BTC is equivalent to the cumulative density function (CDF) of the arrival times of the solute mass ( $F(t)$ ) while its time derivative, which is a concentration rate, is the probability density function (PDF) of the arrival times ( $f(t)$ ). These functions are typically obtained by injecting a pulse in time or a constant concentration at the inlet (or an injection point). Due to the linearity of the advection-diffusion equation, the system is fully characterised by the solution in time of a single injection (i.e. its Green's function).

To enable the comparison between simulations considering different parameters and different durations, we consider a dimensionless time  $T$  obtained by dividing  $t$  by the average travel time, calculated as the ratio between the longitudinal domain dimension and the average fluid velocity. This quantity is equivalent to the injected pore volume. The section averaged concentration at the outlet is non-dimensionalised by dividing it by the fixed single inlet concentration and is represented by  $\bar{c}$ .

In the post processing phase of the simulation results, the following quantities were estimated:



***Péclet number***

$$Pe_x [-] = \frac{\overline{v_x} \lambda_x}{D_{mol}}; \quad (11)$$

***effective permeability***

$$k_x^{eff} [m^2] = -\frac{\overline{v_x} \mu}{\frac{\partial p}{\partial x} - \rho g}; \quad (12)$$

***nominal macrodispersion***

$$D_{mac}^{ij} [m^2/s] = \phi \boldsymbol{\lambda}^T \mathbf{V} \quad (13)$$

where  $\boldsymbol{\lambda}$  and  $\mathbf{V}$  are typical lengths and velocity vectors. Equation (13) allows the macrodispersion matrix to be approximated a priori starting from geo-statistical (correlation length  $\boldsymbol{\lambda}$ ) and flow (velocity  $\mathbf{V}$ ) data, independent of the BTC data. Concentration data coming from the BTC constitutes the basis for the methods adopted to estimate the macrodispersion a posteriori, as illustrated in section 2.5.1.

### 2.5.1 Breakthrough curve and inverse Gaussian approximation

The mass arrival time distribution simulated with the one-dimensional advection-dispersion equation is the inverse Gaussian distribution. This corresponds to the analytical solution of eq. (10) in a semi-infinite one-dimensional domain with a Dirac-delta initial condition. For practically relevant parameters, this is almost indistinguishable from the solution on a finite domain with a Dirac-delta (in time) concentration injection at the inlet. For our problem with a continuous injection at the inlet, due to the linearity of the problem, the BTC is well approximated by the integral in time of the Inverse Gaussian distribution, computed for a fixed section in space (the outlet in our case). When transport behaviour is Fickian, we can approximate the experimental BTCs with the cumulative density function of the Inverse Gaussian distribution as

$$F(T; \mu_1, \nu) = \bar{c} = \Phi \left( \sqrt{\frac{\nu}{T}} \left( \frac{T}{\mu_1} - 1 \right) \right) + e^{\frac{2\nu}{\mu_1}} \Phi \left( -\sqrt{\frac{\nu}{T}} \left( \frac{T}{\mu_1} + 1 \right) \right) \quad (14)$$

where  $\Phi$  is the standard normal cumulative distribution function,  $\mu_1$  is the first order statistical moment of the concentration rate distribution and  $\nu$  is a shape parameter. The PDF of the solute arrival times can be obtained through a time derivative of (14) and corresponds to the PDF of the solute arrival times. This PDF is expressed as [41]

$$f(T; \mu_1, \nu) = \frac{\partial \bar{c}}{\partial T} = \sqrt{\frac{\nu}{2\pi T^3}} \exp \left[ -\frac{\nu(T - \mu_1)^2}{2\mu_1^2 T} \right]. \quad (15)$$

Other analytical solutions are available for different boundary conditions on finite domains [42]. For the purposes of this paper, we will only consider the

Inverse Gaussian model as a reference for Fickian transport due to its simpler analytical formula more suitable to fitting and moment matching. The inverse Gaussian is generally a good approximation [43] for macro-dispersion in heterogeneous media if

- domain is large;
- experiment time is long;
- domain's properties are ergodic.

The PDF of mass arrival times from numerical experiments that follow a Fickian model are clearly distinguishable by a short and exponential-like tail as  $t \rightarrow \infty$ . Non-Fickian transport processes have a clear impact on the shape of the PDF of the arrival times: early arrival concentrations raise the PDF peak and power law scaling emerges prior to exponential decay [17, 43]. of the domain, the last part of the curve will always follow an exponential-like trend because it represents the filling of the slowest remaining regions by pure diffusion.

### ***The moments' method***

Moments of the numerically computed BTC can be matched with the ones from the cumulative Inverse Gaussian distribution. Following [44, 45], the estimation of the statistical moments of the cumulative Inverse Gaussian is performed by approximating its parameters  $\mu_1$  and  $\nu$  as

$$E[\bar{c}] = \mu_1 \quad (16)$$

$$Var[\bar{c}] = \mu_2 - \mu_1^2 = \frac{\mu_1^3}{\nu}. \quad (17)$$

To compute the first and second order moments we used

$$\begin{aligned} \mu_1 &= \int_0^{+\infty} fTdT = \int_0^{+\infty} F'TdT = - \int_0^{+\infty} FdT + [FT]_0^{+\infty} \\ &= - \sum_{i=0}^{+\infty} F_i\Delta T + F_{+\infty}T_{+\infty}, \end{aligned} \quad (18)$$

$$\begin{aligned} \mu_2 &= \int_0^{+\infty} fT^2dT = \int_0^{+\infty} F'T^2dT = -2 \int_0^{+\infty} FTDdT + [FT^2]_0^{+\infty} \\ &= -2 \sum_{i=0}^{+\infty} F_iT_i\Delta T + F_{+\infty}T_{+\infty}^2. \end{aligned} \quad (19)$$

The estimated effective velocity and macrodispersion coefficient can be estimated from statistical moments as

$$V_x = \frac{L_x}{\mu_1} \quad (20)$$

$$D_{xx}^{mac} = \frac{\mu_2 V^3}{2L_x} \quad (21)$$

where  $L_x$  is the distance between the inlet and outlet sections (in our case the domain length). To quantify the distance between the numerical outputs and the Inverse Gaussian approximation, a normalised error  $e$  was defined as

$$e = \frac{\bar{c}(T) - F(T)}{\bar{c}(T)} \cdot 100. \quad (22)$$

### ***Least squares estimation***

Parameter estimation is performed by minimising the least squared error between numerical data and the models (14)-(15). Under the assumption of identically distributed and uncorrelated errors this procedure corresponds to a maximum likelihood estimation. This procedure is applied to three types of data

- probability density function of the concentration distribution, obtained by numerical differentiation of the BTC values at the outlet;
- cumulative density function of the concentration arrival times (i.e. the BTC);
- small subset of concentration data which spans 0.5 dimensionless time unit and it is centered around the peak of the probability density function.

In the first and third case, the analytical function used as reference to perform the least squares fitting is the probability density function of the inverse Gaussian distribution given by equation (15) while for the second case the analytical function is equation (14). For all cases the analysis was performed using Python library `lmfit` constraining the estimation so that  $\mu_1$  and  $\nu$  were always non-negative. Values of the estimated parameters uncertainty are also obtained from the diagonal entries of the parameters covariance matrix computed by `lmfit` and were used to assess the reliability of the estimate. The initial values for the least square estimation were set equals to values computed for  $\mu_1$  and  $\nu$  with the moments' method.

## **3 Numerical experiments**

Geostatistical, flow and transport numerical simulations were conducted over hexahedral domains which represent a portion of the subsurface with dimensions  $(L_x/l, L_y/l, L_z/l) = (2, 1, 1)$  where  $L_i$  are the dimensions of the domain and we took  $l = L_y = L_z$  as the reference length. The mesh is unstructured and characterised by cubic cells of dimension  $d/l = 0.05$ , so that the total number of cells is  $2 \cdot 10^6$ .

The permeability distribution within the domain corresponds to the field generated with a PGS simulation while porosity is assumed homogeneous over the domain. All the simulated fields considered in this study share the correlation function reported in equation (2), the number of permeability zones, as well as the volumetric proportion for each of the facies (see table 1). We

investigate the variability of the observed output and of the estimated parameters as a function of three inputs: geostatistical parameters (e.g., correlation length used to generate the conductivity fields), hydraulic properties (i.e., permeability) and transport regime, defined in terms of  $Pe$ .

Based on the assigned permeability values, we distinguish two cases: low and high contrast. For both cases the permeability values  $k_i$  assigned to the four geomaterials considered are evenly spaced on a logarithmic scale. However, for the low permeability contrast case the four permeability values range between  $10^{-10}$  and  $10^{-13} \text{ m}^2$  with a relative ratio  $\log_{10}(k_i/k_{i+1}) = 1$  while for the high permeability contrast case permeability values range between  $10^{-9}$  and  $10^{-15} \text{ m}^2$  and  $\log(k_i/k_{i+1}) = 2$ . Boundary conditions for the pressure are set as zero gradient along the lateral boundaries and a one dimensional pressure gradient of  $50 \text{ Pa/m}$  aligned with the longitudinal direction. Concentration boundary conditions are fixed single concentration on the inlet boundary and zero gradient on all the other sides. This type of injection is described by a step function.

Geostatistical parameters	
Correlation function	Exponential
Number of facies	4
Volumetric proportion	25%
Flow parameters	
Pressure gradient [Pa/m]	50
Transport parameters	
Fixed inlet concentration [-]	1

**Table 1** Parameters kept constant throughout the simulations.

The simulation workflow is divided into three steps

- geostatistics: the permeability domain is generated using the truncated pluri-Gaussian algorithm;
- flow: equation 5 is solved with the prescribed boundary conditions and provides the steady state flow field;
- transport: advection-dispersion transient model is solved with continuous injection for each simulation time step.

The simulations are run within the open-source OPENFOAM<sup>®</sup>-based library SECUREFoam [24] which includes the `setRandomField` utility for truncated pluri-Gaussian simulations, `simpleDarcyFoam` and `adaptiveScalarTransportFoam` solvers for flow and transport simulations. Most of the simulations were run in parallel on 96 cores split between 8 HPC nodes. An adaptive time step tied to the Courant number was implemented together with an automatic check on the section-average outlet concentration value which stopped the transport simulation when a value of 0.99 on the outlet boundary was reached. In this setting, the overall simulation time ranges between 1 and 7 hours depending on the permeability contrast adopted, with

high contrast cases being characterised by larger CPU costs. Transport simulation are the most expensive of the three simulation steps, accounting for between the 70 and 95 % of the computational time, depending on the low or high permeability contrast setting.

## 4 Results

The results presented in this section aim to assess the impact of the parameters related to the PGS fields on solute transport processes. To this end, first, we first compare the PDFs of velocity point values obtained in the considered fields. Then, we move to the analysis of the transport simulations and we provide a qualitative assessment of the variability exhibited by results obtained from realisations of the conductivity fields generated with identical geostatistical parameters (section 4.2). Finally, we analyse the impact of three physical parameters on PDFs, namely permeability contrast (section 4.3), the longitudinal correlation length used to generate the fields (section 4.4) and Péclet number (section 4.5). By testing transport behaviour in settings with increasing longitudinal correlation lengths and permeability contrast between facies, we aim to:

- assess the sensitivity of transport behaviour and the onset of non-Fickian transport with respect to the correlation length and permeability constast of the generated permeability fields;
- quantify the discrepancy from Fickian behaviour as a function of both correlation lengths and permeability contrast, considered separately.

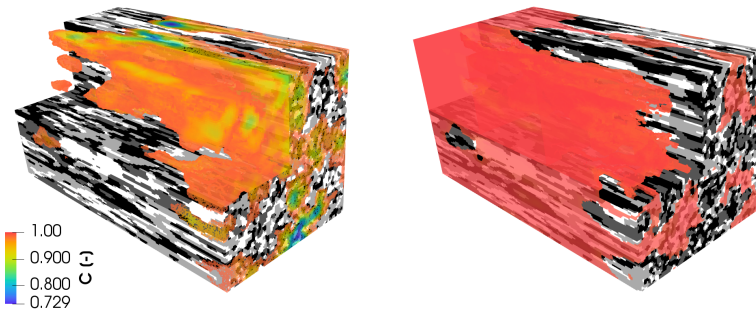


**Fig. 2** Solute plume distribution in high contrast permeability domain at late time. Domain sizes are  $2 \times 1 \times 1$  and correlation lengths along the three directions are set to  $(0.8, 0.1, 0.1)$ . On the left panel it is possible to observe how low solute concentration values (0 blue - 0.99 red) are confined to low permeability regions ( $10^{-12} [m^2]$  dark grey -  $10^{-13} [m^2]$  black) while on the right panel high concentration values (0.99 blue - 1.00 red) are highlighted and their spatial distribution clearly show that saturated zones are concentrated in highly permeable regions ( $10^{-10} [m^2]$  dark grey -  $10^{-11} [m^2]$  black).

Before moving to these detailed analyses, figure 2 illustrates the simulation of the solute plume at late times through a PGS field with high contrast

permeability and characterised by longitudinal correlation length of 0.8 m. Figure 2 on the left highlights the regions where concentration values falls beneath the 0.99 threshold while the right panel visualises the regions where concentration values fall between 0.99 and 1. It is possible to observe that the transport of the solute is facilitated in the high permeable regions of the domain (white and light grey) while low permeability ones (dark grey and black) form a flow barrier that impede advective solute transport.

## 4.1 Velocity PDFs

The velocity PDF has a direct influence on non-Fickian transport features [46]. The PDFs of point velocity values with increasing longitudinal correlation lengths  $\lambda_x$  are shown in figure 3. The longitudinal velocity  $V_x$  normalised with the average longitudinal velocity is reported on the horizontal axis of figures 3 and 4 as  $V_x^*$ . The vertical axis of figure 3 reports the probability density distribution as a function of the longitudinal velocity  $p(V_x^*)$ . As expected, the velocity distributions in figure 3 are comparable for different correlation lengths as they all show four peaks of similar height corresponding to the four facies that populate the domain. However, as the correlation length increases, the peaks become sharper reflecting the formation of preferential flow paths where velocities are lumped around the mean velocity of a given facies, each corresponding to a mode of the distributions (figure 4). This result also indicates that with a decrease of  $\lambda_x$  the distribution of velocity values progressively converges towards a uniform distribution across the whole range. Comparing the amplitude of the peaks in the two panels of figure 3 we observe that as the permeability contrast increases the four modes of the distribution appear more distinct for high contrast than for low contrast. Note also that the high contrast distribution spans a much wider interval of velocity values as compared to the low contrast one.

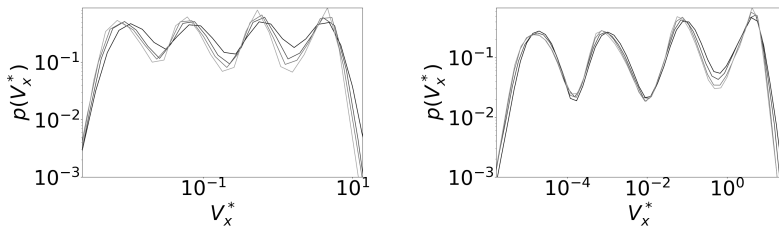


**Fig. 3** PDFs of the longitudinal velocity component for low and high contrast. Velocity PDFs are shown for low (left) and high (right) permeability contrast. The correlation lengths  $\lambda_x$  span between 0.4 (darker lines) and 1.0 (lighter lines).

Figure 4 reports the conditional PDFs  $p(V_x^*|k = k_i)$ , where each distribution considers only longitudinal velocities values computed in cells associated with a given facies ( $i = 1 \dots 4$ ). Velocities in highly permeable regions show an

asymmetric distribution, characterised by a pronounced peak and a leftward tail. Conversely, velocity values observed in the low permeability regions tend to assume a symmetric and compact distribution. This distinct behavior is particularly evident in high contrast media. This means that high-permeability regions may feature a broad distribution of velocity values because of the overall connectivity of the field. Highly connected regions give rise to fast channels in formations featuring large values of  $k$  but poorly connected regions may also involve high-permeability cells.

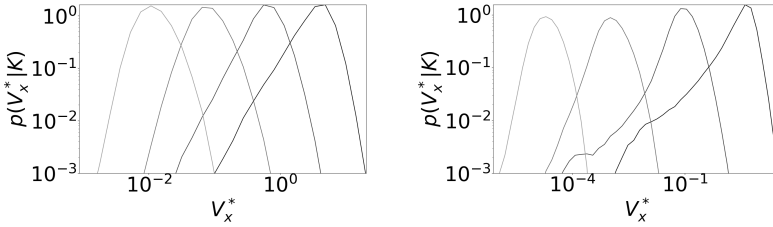


**Fig. 4** Conditional PDFs of the longitudinal velocity values in low (left) and high (right) permeability contrast. Results are shown for correlation lengths  $\lambda_x = 0.4$ . The curves are shown with different colors depending on the facies permeability, i.e., lighter colors correspond to low permeability and darker colors to high permeability media.

## 4.2 Variability of transport behaviour across multiple realizations

Figure 5 displays the overlap of the PDF of the solute arrival times, obtained taking the time derivative of the BTC ( $d\bar{c}/dT$ ) obtained from 10 realisations of permeability fields generated with the same geostatistical parameters. The observed variability tends to be greater for early times while at later times the different realizations attain similar values. This behaviour is the result of the solute exploring more broadly the facies' heterogeneities as the solute fill the whole domain. Although the outlined behaviour does not show qualitatively relevant differences between low (left panel) and high (right panel) permeability contrast, for high permeability contrast the spread between the first part of the curves is greater than the spread for low permeability contrast. Because in the following we focus on the assessment of the macroscopic response of the system and the departure from a Fickian macrodispersive model, we deem a single realisation to be representative of the response of the system to various combinations of the investigated parameters.

## 4.3 Effect of permeability contrast

Figure 6 illustrates the effect of the permeability contrast between facies on transport, by comparing the results of transport simulations performed on two geological domains with identical arrangement but assuming low and high

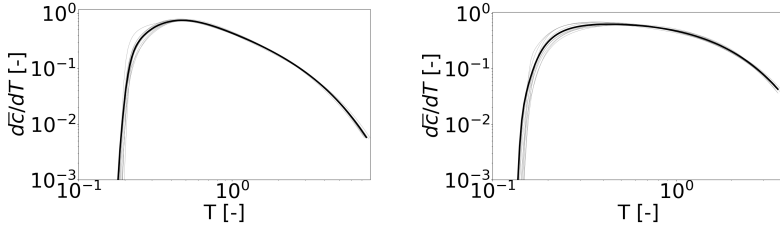


**Fig. 5** PDFs of solute arrival times associated with 10 realisations with the same correlation length ( $\lambda_x = 0.8m$ ). Low and high permeability contrast on the left and right side of the panel respectively.

permeability contrast. Geostatistical, flow and transport parameters relative to the results in figure 6 are shown in table 2.

The simulated BTCs (i.e., CDFs of the solute arrival times) are shown on top left of figure 6 while on top right of figure 6 the corresponding time derivative are shown, these latter corresponding to the PDFs of arrival times. A Fickian model based on the inverse Gaussian distribution yields a reasonable fitting of the numerical data for the low contrast simulation, where the difference between one facies' permeability and another remains within one order of magnitude (see figure 6, bottom left). In this case the match between the numerical simulation and the Inverse Gaussian distribution is satisfactory especially for the peak and the right tail of the distribution. Conversely, early arrival times are not well approximated by the Fickian model. In the low contrast case the results obtained with different estimation methods are self-consistent, i.e. least squares and moments methods yield similar outcomes. If the contrast in permeability increases, the Inverse Gaussian distribution cannot match the simulated data (figure 6, bottom right), regardless of the method used to estimate its parameters (Least Square or Moments method).

In summary, figure 6 suggests that as the permeability contrast increases, the evolution of the solute concentration shows significant departure from the Fickian model.

	Low contrast	High contrast
<b>Geostatistical parameters</b>		
$\lambda_x$ [m]	0.8	0.8
$\log(k_{i+1}/k_i)$ [-]	1	2
$Var(\log(k))$ [ $\log m^4$ ]	6.5	26.1
<b>Flow parameters</b>		
$k_{eff,x}$ [ $m^2$ ]	$2.11 \cdot 10^{-11}$	$1.49 \cdot 10^{-10}$
$\bar{V}_x$ [m/s]	$1.07 \cdot 10^{-6}$	$9.64 \cdot 10^{-6}$
$Pe_x$ [-]	21113	59633

**Table 2** Geostatistical and flow parameters for the low and high permeability contrast fields used to generate results reported in Figure 6. The flow parameters were defined by equations (11) and (12).



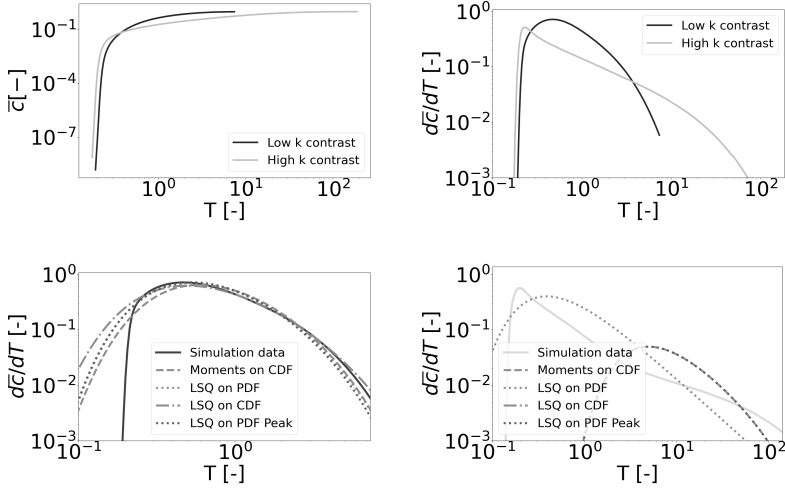


**Fig. 6** Top panels: breakthrough curves (left) and their time derivatives (right) simulated on identical geological structure with low and high permeability contrast between the facies. Bottom panels: the curves are overlapped with the corresponding Inverse Gaussian approximations via least square (LSQ) or moments' method estimation in low (left) and high (right) permeability contrast case.

A detailed analysis of these results is shown in Table 3. Numerical results confirm that the relative error between Inverse Gaussian approximations and the numerical solution is significantly lower for low permeability contrast than for high permeability contrast. It is then possible to conclude that the level of accuracy of macrodispersion models in capturing transport behaviour decreases with the permeability contrast. Table 3 reports the values of macrodispersion parameters computed through approximation (13) (considered as a reference value) and compare them with the the estimated ones. Transport parameters estimations are closer to the reference values for the low contrast if compared to the high contrast cases. Moreover the estimates obtained through least squares in the high contrast case are generally affected by large confidence bounds (i.e., they are indicated in *italic*) indicating that the estimated values cannot be considered as reliable.

#### 4.4 Correlation length

Transport simulations are performed on PGS domains sharing comparable geostatistical parameters (table 4) while increasing longitudinal correlation lengths (figure 7). These provide interesting insights into the transition from Fickian to anomalous transport in relation to the connectivity degree of the sediment structure (figure 8). We emphasize here that the correlation length mentioned here is the one employed to generate the continuous Gaussian random fields which are then employed to generate the conductivity fields (see

	Low contrast			High contrast		
	$\bar{V}_x[m/s]$	$D_{mac}[m^2/s]$	$e[\%]$	$\bar{V}_x[m/s]$	$D_{mac}[m^2/s]$	$e[\%]$
<i>Reference solution</i>	$1.07 \cdot 10^{-6}$	$8.57 \cdot 10^{-7}$	—	$9.64 \cdot 10^{-6}$	$7.71 \cdot 10^{-6}$	—
<i>Method 1</i>	$6.94 \cdot 10^{-7}$	$4.97 \cdot 10^{-7}$	16.20	$7.03 \cdot 10^{-7}$	$1.59 \cdot 10^{-6}$	79.5
<i>Method 2</i>	$2.08 \cdot 10^{-7}$	$1.81 \cdot 10^{-7}$	10.71	<i><math>3.79 \cdot 10^{-5}</math></i>	<i><math>8.79 \cdot 10^{-7}</math></i>	<i>48.1</i>
<i>Method 3</i>	$6.50 \cdot 10^{-7}$	$6.09 \cdot 10^{-7}$	11.94	$6.36 \cdot 10^{-7}$	$2.33 \cdot 10^{-6}$	126.7
<i>Method 4</i>	$2.42 \cdot 10^{-7}$	$1.13 \cdot 10^{-7}$	11.93	<i><math>8.95 \cdot 10^{-8}</math></i>	<i><math>3.74 \cdot 10^{-5}</math></i>	<i>49.2</i>

**Table 3** Simulated (*Reference solution*) and estimated (*Methods 1 – 4*) values for average Darcy velocity  $\bar{V}_x$ , macrodispersion  $D_{mac}$  and relative breakthrough error  $e$  values. The *reference solution* values represent the average longitudinal velocity and the nominal macrodispersion as from equation (13). *Method 1* is the moments method, *Method 2*, 3 and 4 correspond to least squares method applied to the simulated PDF, CDF and the PDF peak data. As a result of the unsuitability of the Inverse Gaussian model to the describe the PDF in high permeability contrast scenarios, some values (*italic*) are characterised by extremely large standard deviations ( $\sigma > 10^6$ ).

Figure 1). This length can be interpreted as the characteristic length over which facies' transitions are observed.

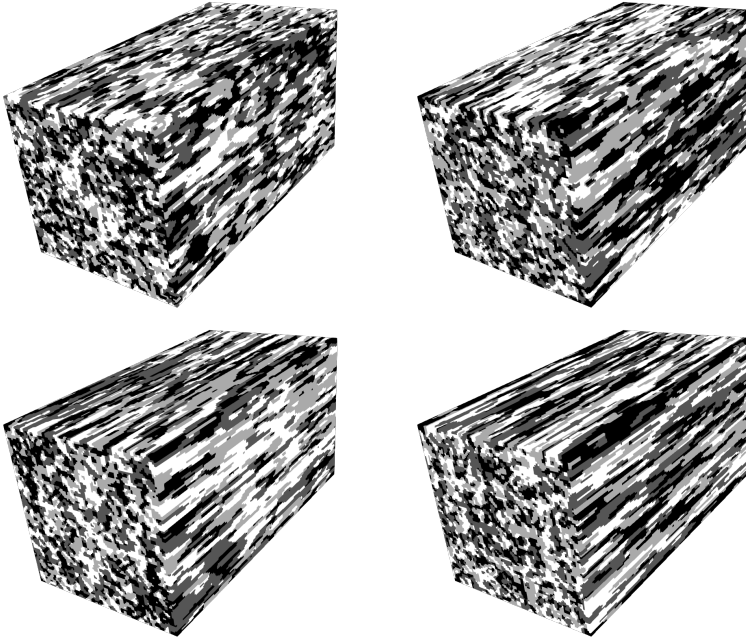


**Fig. 7** Truncated pluri-Gaussian permeability fields with increasing longitudinal correlation length  $\lambda_x$ . Clockwise order from top left panel:  $\lambda_x = 0.4$ ,  $\lambda_x = 0.6$ ,  $\lambda_x = 0.8$ ,  $\lambda_x = 1.0$ .

Figure 8 displays the PDFs of the solute arrival times obtained for a range of values assigned to  $\lambda_x$ . As the longitudinal correlation length increases, the magnitude of the peak value increases and the peak shifts towards earlier arrival times. This can be explained observing that, with increasing correlation in the longitudinal direction, the connectivity between highly permeable facies

favours the formation of fast channels where advection prevails over diffusion thus leading to early arrivals. This effect is more evident for the high contrast scenario (right side of figure 8) and is reflected by the solute arrivals PDFs trends: as the domain connectivity increases, the initial concentration peak rises while the central segment of the curve highlights a power law response.

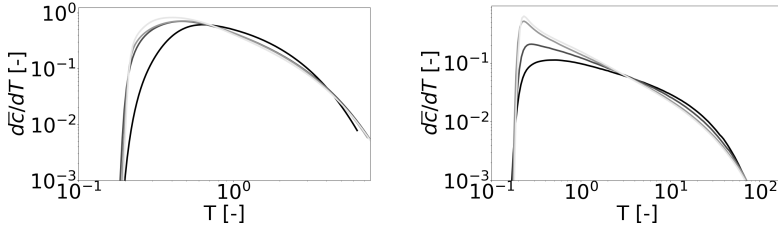


**Fig. 8** Arrival time PDFs computed as  $d\bar{c}/dT$  for low (left panel) and high (right panel) permeability contrast for as a function of the longitudinal correlation length  $\lambda_x$ . From the darkest to the lightest curve the longitudinal correlation length  $\lambda_x = 1$  increases with evenly spaced interval from 0.4 to 1.

Tables 4 and 5 report relevant geostatistical and flow simulation parameters which are required to interpret the results of the average Darcy velocity and macrodispersion estimation process provided in tables 6 and 7. As a result of the emergence of preferential flow-paths, the effective permeability shows a positive trend for increasing correlation lengths.

	$\lambda_x = 0.4$	$\lambda_x = 0.6$	$\lambda_x = 0.8$	$\lambda_x = 1.0$
<i>Geostatistical parameters</i>				
$\log(k_i/k_{i+1})$	1	1	1	1
$Var(\log(k)) [\log m^4]$	6.7	6.6	6.6	6.6
<i>Flow parameters</i>				
$k_{eff,x} [m^2]$	$1.75 \cdot 10^{-11}$	$1.99 \cdot 10^{-11}$	$2.14 \cdot 10^{-11}$	$2.27 \cdot 10^{-11}$
$Pe_x [-]$	3508	5972	8571	11355

**Table 4** Geostatistical and flow parameters for low permeability contrast simulations. The flow parameters are defined by equations (11) and (12).

	$\lambda_x = 0.4$	$\lambda_x = 0.6$	$\lambda_x = 0.8$	$\lambda_x = 1.0$
<i>Geostatistical parameters</i>				
$\log(k_i/k_{i+1})$	2	2	2	2
$Var(\log(k)) [\log m^4]$	26.1	26.2	25.9	26.2
<i>Flow parameters</i>				
$k_{eff,x} [m^2]$	$1.50 \cdot 10^{-10}$	$1.76 \cdot 10^{-10}$	$1.93 \cdot 10^{-10}$	$2.05 \cdot 10^{-10}$
$Pe_x [-]$	29953	52919	77127	102719

**Table 5** Geostatistical and flow parameters' for high permeability contrast simulations. The flow parameters were defined by equations (11) and (12) and are computed in the longitudinal direction of the flow. Longitudinal correlation length increases from 0.4 to 1.0.

Comparing the relative error computed for low and high permeability contrast cases, it is clear that the reliability of the Fickian model at the macroscale decreases with the permeability contrast (see figure 9). We also observe a mild increasing trend of the relative error with increasing values of the correlation length. This trend is justified by the role of the preferential flow-paths which facilitate fast advective flow that make overall solute behaviour anomalous.

### Low contrast

	$\lambda_x = 0.4$				$\lambda_x = 0.6$				$\lambda_x = 0.8$				$\lambda_x = 1.0$			
	$\bar{V}_x [m/s]$	$D [m^2/s]$	$e [\%]$	$\bar{V}_x [m/s]$	$D [m^2/s]$	$e [\%]$	$\bar{V}_x [m/s]$	$D [m^2/s]$	$e [\%]$	$\bar{V}_x [m/s]$	$D [m^2/s]$	$e [\%]$	$\bar{V}_x [m/s]$	$D [m^2/s]$	$e [\%]$	$e [\%]$
<i>Ref. s.</i>	$8.77 \cdot 10^{-7}$	$3.51 \cdot 10^{-7}$	—	$9.95 \cdot 10^{-7}$	$5.97 \cdot 10^{-7}$	—	$1.07 \cdot 10^{-6}$	$8.56 \cdot 10^{-7}$	—	$1.14 \cdot 10^{-6}$	$1.14 \cdot 10^{-6}$	—	$1.14 \cdot 10^{-6}$	$1.14 \cdot 10^{-6}$	—	—
<i>M. 1</i>	$5.39 \cdot 10^{-7}$	$2.68 \cdot 10^{-7}$	12.9	$6.26 \cdot 10^{-7}$	$4.54 \cdot 10^{-7}$	16.3	$6.94 \cdot 10^{-7}$	$4.97 \cdot 10^{-7}$	16.2	$7.60 \cdot 10^{-7}$	$6.15 \cdot 10^{-7}$	19.1	$7.60 \cdot 10^{-7}$	$6.15 \cdot 10^{-7}$	19.1	19.1
<i>M. 2</i>	$1.30 \cdot 10^{-6}$	$6.18 \cdot 10^{-8}$	7.3	$1.91 \cdot 10^{-6}$	$1.68 \cdot 10^{-7}$	11.0	$2.08 \cdot 10^{-6}$	$1.81 \cdot 10^{-7}$	10.7	$2.48 \cdot 10^{-6}$	$2.32 \cdot 10^{-7}$	16.7	$2.48 \cdot 10^{-6}$	$2.32 \cdot 10^{-7}$	16.7	16.7
<i>M. 3</i>	$5.12 \cdot 10^{-7}$	$3.17 \cdot 10^{-7}$	28.2	$5.87 \cdot 10^{-7}$	$5.55 \cdot 10^{-7}$	11.8	$6.50 \cdot 10^{-7}$	$6.09 \cdot 10^{-7}$	11.9	$7.10 \cdot 10^{-7}$	$7.60 \cdot 10^{-7}$	15.8	$7.10 \cdot 10^{-7}$	$7.60 \cdot 10^{-7}$	15.8	15.8
<i>M. 4</i>	$2.03 \cdot 10^{-6}$	$1.31 \cdot 10^{-7}$	23.7	$2.32 \cdot 10^{-6}$	$1.27 \cdot 10^{-7}$	13.0	$2.41 \cdot 10^{-6}$	$1.13 \cdot 10^{-7}$	11.9	$2.68 \cdot 10^{-6}$	$1.17 \cdot 10^{-7}$	16.4	$2.68 \cdot 10^{-6}$	$1.17 \cdot 10^{-7}$	16.4	16.4

**Table 6** Simulated (*Reference solution*) and estimated (*Methods 1 – 4*) values for average Darcy velocity  $\bar{V}_x$ , macrodispersion  $D_{mac}$  and relative breakthrough error  $e$  values in low permeability contrast simulations. *Method 1* is the moments method, *Method 2*, 3 and 4 correspond to least squares method applied to the simulated PDF, CDF and the PDF peak data.

### High contrast

	$\lambda_x = 0.4$				$\lambda_x = 0.6$				$\lambda_x = 0.8$				$\lambda_x = 1.0$			
	$\bar{V}_x [m/s]$	$D [m^2/s]$	$e [\%]$	$\bar{V}_x [m/s]$	$D [m^2/s]$	$e [\%]$	$\bar{V}_x [m/s]$	$D [m^2/s]$	$e [\%]$	$\bar{V}_x [m/s]$	$D [m^2/s]$	$e [\%]$	$\bar{V}_x [m/s]$	$D [m^2/s]$	$e [\%]$	$e [\%]$
<i>Ref. s.</i>	$7.49 \cdot 10^{-6}$	$3.00 \cdot 10^{-6}$	—	$8.82 \cdot 10^{-6}$	$5.29 \cdot 10^{-6}$	—	$9.65 \cdot 10^{-6}$	$7.72 \cdot 10^{-6}$	—	$1.03 \cdot 10^{-6}$	$1.03 \cdot 10^{-6}$	—	$1.03 \cdot 10^{-6}$	$1.03 \cdot 10^{-6}$	—	—
<i>M. 1</i>	$4.89 \cdot 10^{-7}$	$6.27 \cdot 10^{-7}$	62.5	$6.02 \cdot 10^{-7}$	$1.05 \cdot 10^{-6}$	72.8	$7.03 \cdot 10^{-7}$	$1.60 \cdot 10^{-6}$	79.5	$8.08 \cdot 10^{-7}$	$1.91 \cdot 10^{-6}$	80.3	$8.08 \cdot 10^{-7}$	$1.91 \cdot 10^{-6}$	80.3	80.3
<i>M. 2</i>	$1.52 \cdot 10^{-5}$	$9.08 \cdot 10^{-7}$	44.2	$2.56 \cdot 10^{-5}$	$1.58 \cdot 10^{-6}$	54.01	$3.79 \cdot 10^{-5}$	$8.79 \cdot 10^{-7}$	48.1	$4.02 \cdot 10^{-5}$	$8.32 \cdot 10^{-7}$	42.9	$4.02 \cdot 10^{-5}$	$8.32 \cdot 10^{-7}$	42.9	42.9
<i>M. 3</i>	$4.51 \cdot 10^{-7}$	$8.57 \cdot 10^{-7}$	87.6	$5.52 \cdot 10^{-7}$	$1.46 \cdot 10^{-6}$	108.8	$6.36 \cdot 10^{-7}$	$2.34 \cdot 10^{-6}$	126.7	$7.24 \cdot 10^{-7}$	$2.94 \cdot 10^{-6}$	130.1	$7.24 \cdot 10^{-7}$	$2.94 \cdot 10^{-6}$	130.1	130.1
<i>M. 4</i>	$4.89 \cdot 10^{-7}$	$6.27 \cdot 10^{-7}$	70.4	$6.02 \cdot 10^{-7}$	$1.05 \cdot 10^{-6}$	59.2	$8.95 \cdot 10^{-8}$	$3.74 \cdot 10^{-5}$	49.2	$4.22 \cdot 10^{-5}$	$3.53 \cdot 10^{-7}$	43.1	$4.22 \cdot 10^{-5}$	$3.53 \cdot 10^{-7}$	43.1	43.1

**Table 7** Simulated (*Reference solution*) and estimated (*Methods 1 – 4*) values for average Darcy velocity  $\bar{V}_x$ , macrodispersion  $D_{mac}$  and relative error  $e$  values obtained for high permeability contrast simulations. *Method 1* is the moments method, *Methods 2*, 3 and 4 correspond to least squares method applied to the simulated PDF, CDF and the PDF peak data.

Summarizing the results of our numerical experiments, we can say that both correlation length and permeability contrast are triggering factors for non-Fickian transport behaviour. However, the impact of the correlation length on transport becomes more evident as the permeability contrast increases.

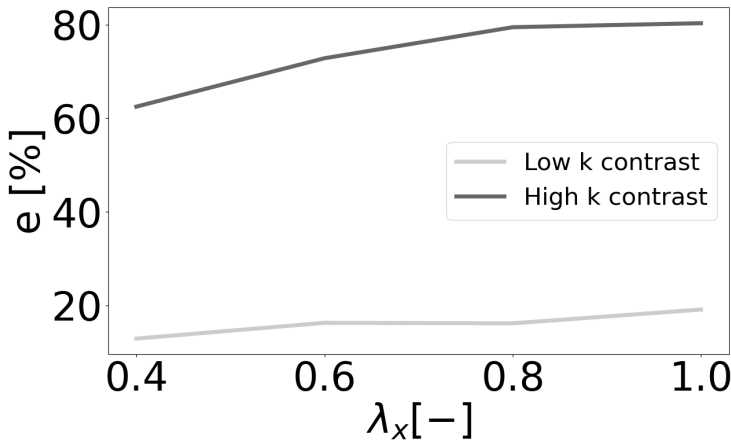


**Fig. 9** Longitudinal correlation length vs relative error computed as the departure from Fickian model (eq. 22) with parameters estimated with the moments method (Method 1).

## 4.5 Effect of Péclet

We analyse here the effect of the Péclet number on our results. This means that not only the effect of different permeability fields (as in section 4.3) or correlation lengths (section 4.4) were tested, but also the effect of different solute composition is considered. This was performed by changing the molecular diffusion coefficient while keeping the average Darcy velocity and the correlation length  $\lambda_x$  constant. Our tests were conducted by varying the Péclet ( $Pe$ ) of each simulation by one order of magnitude. The variations in  $Pe$  have a marked influence on the right tail of the arrival times distributions, as shown in 10. This result can be explained observing that diffusion effects become apparent in late arrivals, while early arrivals are conversely driven by advection-dominated processes. Left and right panels in figure 10 show the combined effect of increasing Péclet (darker to lighter curves) in a low (left) and high (right) permeability contrast domain. The analysis of PDF curves for increasing Péclet yields comparable conclusions with the ones obtained in section 4.4: while the interplay between increasing Péclet numbers and the departure from Fickian behaviour is clear, the increase of permeability contrast still appears to play a predominant role.

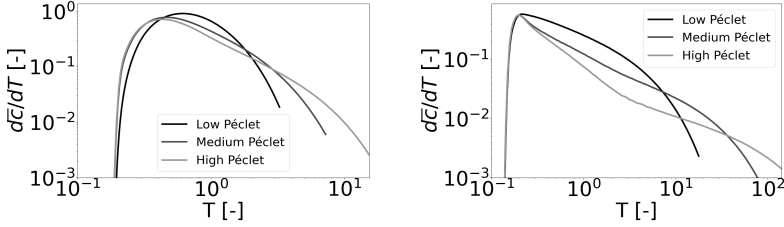


**Fig. 10** Arrival times PDFs in low (left) and high (right) permeability contrast domains sharing the same geological structure ( $\lambda_x = 0.8\text{m}$ ) while characterised by a different Péclet. In case of low permeability contrast, the Péclet number ranges between  $8 \cdot 10^2$  and  $8 \cdot 10^4$  while for high permeability contrast the Péclet ranges between  $6 \cdot 10^3$  and  $6 \cdot 10^5$ . Significant Péclet variation for these simulations was obtained by changing the molecular diffusion coefficient.

Figure 11 shows that the increase in permeability contrast by one order of magnitude exhibits a stronger control on transport behaviour than the increase in Péclet number by one magnitude order as for comparable  $Pe$ , the error associated with low permeability contrast simulations (light curve) is always lower than the error associated with the high permeability contrast (dark curve). The method considered for representing the ideal Fickian behaviour ( $F(x)$  in eq. (22)) for the error curves is the statistical moments method (M.1 in tables 6 and 7).

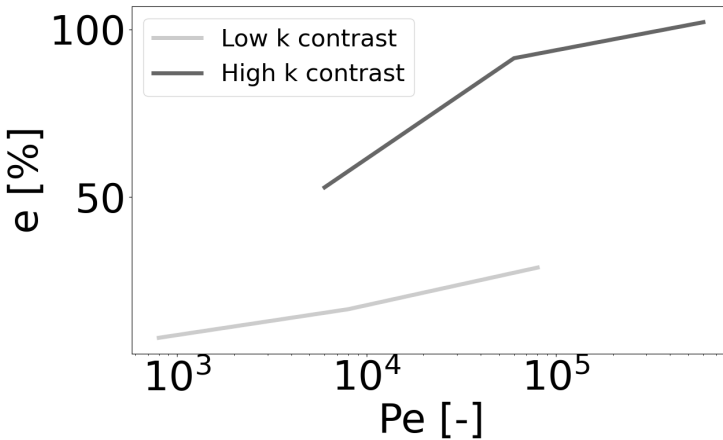


**Fig. 11** Péclet number vs relative error computed as in eq. (22). The interplay between increasing Péclet numbers, permeability contrast and relative error is qualitatively similar to the one exhibited by the increasing longitudinal correlation length in fig. 8.

## 5 Conclusions

In this work we have explored the emergence of non-Fickian transport in random discontinuous permeability fields. These fields have a high degree of geological realism and present some relevant non-Fickian triggering features such as sharp contrast between facies and high connectivity degree. In particular, long channels enhance spatial velocity correlation and the larger and longer the correlated structures are, the more anomalous the transport will appear, with characteristics such as sharp concentration peak or early arrivals.

Flow and transport simulations have been performed over four sets of geological domains varying the assumed permeability contrast, correlation length and Péclet number. We compute the breakthrough curves as the flux-averaged concentration on the outlet section of the domain and analyse them as a key indicator of the transport behaviour. Statistics related to the breakthrough curves quantify the deviation from the advection dispersion model, with parameters calibrated with the method of moments and with global and local (near the peak) least-squares minimisation. We quantify the anomalous transport by comparing the mean square error and the resulting macroscopic parameters. This analysis led to the identification of sharp permeability contrast as the pivotal factor in creating fast flow channels where the solute arrival times tend to anticipate and overestimate the Fickian concentration peak. In fact, while Fickian transport is characterised by a single peak followed by an exponential-like tail, non-Fickian breakthrough curves present variations such as thinner peaks, followed longer power law tails. Our results show that the breakthrough curves trend can be subdivided into three stages: a steep peak of the early arrivals due to the channelling, followed by a power law decay due to the heterogeneous transport velocities, and eventually the exponential-like trend. For moderate permeability contrasts, macrodispersion model can reasonably match only solute transport in low connected porous media. More advanced macro-models are needed to capture transport behaviour in highly connected porous media. The conclusions that can be drawn from the interpretation of these results are:

- flow velocity in low permeability regions is homogeneously distributed around the corresponding peak values. In high permeability regions flow velocities display a left-skewed distribution, indicating the occurrence of low velocity regions in highly permeable media;
- the BTC variability observed between multiple realisations of the same geological setting is more evident at early times while it tends to disappear at late times;
- our results combine error and uncertainty quantification metrics within the physical characterisation of the transport process. Emergence of non Fickian transport is quantified upon relying on relative error with respect to the prediction of a macrodispersive solution, where this latter can be obtained with diverse estimation strategies. Large relative errors and large confidence intervals for estimated parameters are indicative of the unsuitability of the



Inverse Gaussian distribution in interpreting the outcomes of high-resolution numerical simulations, thus indicating non-Fickian features.

- a Fickian macrodispersive model can match with reasonable accuracy solute arrival times in domains featuring conductivity values distributed over up to four orders of magnitudes. In such conditions the Fickian model provides a poor prediction of early arrivals, but can capture with good accuracy the peak and the late arrivals. Overall observed errors are in the order of 10–20 %. Lowest errors are associated with cases where the characteristic size associated with the medium heterogeneity is much smaller than the distance travelled by the solute.
- a hierarchy of non-Fickian triggering factors can be established: permeability contrast plays a primary role in determining the fate of the solute, while correlation length and Péclet number can be both considered secondary non-Fickian transport triggering factors.
- while for Fickian or moderately non-Fickian transport the different parameter estimation methods (method of moments or least-squares-based methods) are equivalent, when a macrodispersion approximation is sought for significantly non-Fickian curves, the choice of the fitting method is crucial as it can lead to very different effective parameters and fitted curves. Although this is expected, due to the lack of validity of the underlying model, it has important practical consequences for practitioners that are nevertheless forced to use and fit macrodispersion effective parameters. Here, the method of moments is built to preserve accurately the statistics but it could significantly mispredict the early arrival peak as well as the long tails.

Future works will include the extension to more realistic injection scenarios, variable density and hydrodynamic dispersion models, investigating the effect of different lithotype rules, as well as interpreting the non-Fickian transport results with more sophisticated anomalous transport models including spatial Markov processes [47] and Generalised Multi-Rate Transfer equations [48].

## Declarations

### Conflict of Interests

The authors have no relevant financial or non-financial interests to disclose.

### Funding

This work was supported by the Royal Society through the grant No. IES\R3\170302.

## Acknowledgements

We would like to especially thank Prof. John Billingham for his insightful suggestions and for his detailed proofreading of this paper.

## References

- [1] Adams, E.E., Gelhar, L.W.: Field study of dispersion in a heterogeneous aquifer: 2. spatial moments analysis. *Water Resources Research* **28**(12), 3293–3307 (1992)
- [2] Barlebo, H.C., Hill, M.C., Rosbjerg, D.: Investigating the macrodispersion experiment (made) site in columbus, mississippi, using a three-dimensional inverse flow and transport model. *Water Resources Research* **40**(4) (2004)
- [3] Fiori, A., Cvetkovic, V., Dagan, G., Attinger, S., Bellin, A., Dietrich, P., Zech, A., Teutsch, G.: Debates—stochastic subsurface hydrology from theory to practice: The relevance of stochastic subsurface hydrology to practical problems of contaminant transport and remediation. what is characterization and stochastic theory good for? *Water Resources Research* **52**(12), 9228–9234 (2016)
- [4] Zinn, B., Harvey, C.F.: When good statistical models of aquifer heterogeneity go bad: A comparison of flow, dispersion, and mass transfer in connected and multivariate gaussian hydraulic conductivity fields. *Water Resources Research* **39**(3) (2003)
- [5] Jankovic, I., Maghrebi, M., Fiori, A., Dagan, G.: When good statistical models of aquifer heterogeneity go right: The impact of aquifer permeability structures on 3d flow and transport. *Advances in water resources* **100**, 199–211 (2017)
- [6] Bianchi, M., Zheng, C.: A lithofacies approach for modeling non-fickian solute transport in a heterogeneous alluvial aquifer. *Water Resources Research* **52**(1), 552–565 (2016)
- [7] Dentz, M., Le Borgne, T., Englert, A., Bijeljic, B.: Mixing, spreading and reaction in heterogeneous media: A brief review. *Journal of contaminant hydrology* **120**, 1–17 (2011)
- [8] Gelhar, L.W., Axness, C.L.: Three-dimensional stochastic analysis of macrodispersion in aquifers. *Water Resources Research* **19**(1), 161–180 (1983)
- [9] Bear, J.: *Hydraulics of Groundwater*. Courier Corporation, ??? (2012)
- [10] de Barros, F.P.J., Guadagnini, A., Riva, M.: Features of transport in non-gaussian random porous systems. *International Journal of Heat and Mass Transfer* **184**, 122244 (2022). <https://doi.org/10.1016/j.ijheatmasstransfer.2021.122244>

- [11] Riva, M., Guadagnini, A., Fernandez-Garcia, D., Sanchez-Vila, X., Ptak, T.: Relative importance of geostatistical and transport models in describing heavily tailed breakthrough curves at the lauswiesen site. *Journal of Contaminant Hydrology* **101**(1-4), 1–13 (2008). <https://doi.org/10.1016/j.jconhyd.2008.07.004>
- [12] Dagan, G.: *Flow and Transport in Porous Formations*. Springer, ??? (2012)
- [13] Hansen, S.K., Haslauer, C.P., Cirpka, O.A., Vesselinov, V.V.: Direct breakthrough curve prediction from statistics of heterogeneous conductivity fields. *Water Resources Research* **54**(1), 271–285 (2018). <https://doi.org/10.1002/2017WR020450>
- [14] Zech, A., Attinger, S., Bellin, A., Cvetkovic, V., Dagan, G., Dentz, M., Dietrich, P., Fiori, A., Teutsch, G.: A comparison of six transport models of the made-1 experiment implemented with different types of hydraulic data. *Water Resources Research* **57**(5), 2020–028672 (2021). <https://doi.org/10.1029/2020WR028672>
- [15] Neuman, S.P., Tartakovsky, D.M.: Perspective on theories of non-fickian transport in heterogeneous media. *Advances in Water Resources* **32**(5), 670–680 (2009)
- [16] Zhang, Y., Green, C.T., Fogg, G.E.: The impact of medium architecture of alluvial settings on non-fickian transport. *Advances in water resources* **54**, 78–99 (2013)
- [17] Edery, Y., Guadagnini, A., Scher, H., Berkowitz, B.: Origins of anomalous transport in heterogeneous media: Structural and dynamic controls. *Water Resources Research* **50**(2), 1490–1505 (2014)
- [18] Edery, Y., Porta, G.M., Guadagnini, A., Scher, H., Berkowitz, B.: Characterization of bimolecular reactive transport in heterogeneous porous media. *Transport in Porous Media* **115**(2), 291–310 (2016). <https://doi.org/10.1007/s11242-016-0684-0>
- [19] Edery, Y., Stolar, M., Porta, G., Guadagnini, A.: Feedback mechanisms between precipitation and dissolution reactions across randomly heterogeneous conductivity fields. *Hydrology and Earth System Sciences* **25**(11), 5905–5915 (2021). <https://doi.org/10.5194/hess-25-5905-2021>
- [20] Mariethoz, G., Renard, P., Cornaton, F., Jaquet, O.: Truncated pluri-gaussian simulations to characterize aquifer heterogeneity. *Groundwater* **47**(1), 13–24 (2009)
- [21] Gotovac, H., Cvetkovic, V., Andricevic, R.: Flow and travel time statistics

- in highly heterogeneous porous media. *Water resources research* **45**(7) (2009)
- [22] Sole-Mari, G., Riva, M., Fernàndez-Garcia, D., Sanchez-Vila, X., Guadagnini, A.: Solute transport in bounded porous media characterized by generalized sub-gaussian log-conductivity distributions. *Advances in Water Resources* **147**, 103812 (2021). <https://doi.org/10.1016/j.advwatres.2020.103812>
  - [23] Bianchi, M., Pedretti, D.: Geological entropy and solute transport in heterogeneous porous media. *Water Resources Research* **53**(6), 4691–4708 (2017)
  - [24] Icardi, M., Pescimoro, E., Municchi, F.: SECURE FOAM. <https://github.com/multi-form-UoN/SECUREFOAM> (2019)
  - [25] Savoy, H., Kalbacher, T., Dietrich, P., Rubin, Y.: Geological heterogeneity: Goal-oriented simplification of structure and characterization needs. *Advances in Water Resources* **109**, 1–13 (2017)
  - [26] Heße, F., Prykhodko, V., Schlüter, S., Attinger, S.: Generating random fields with a truncated power-law variogram: A comparison of several numerical methods. *Environmental modelling & software* **55**, 32–48 (2014)
  - [27] Dimitrakopoulos, R., Luo, X.: Generalized sequential gaussian simulation on group size  $\nu$  and screen-effect approximations for large field simulations. *Mathematical Geology* **36**(5), 567–591 (2004)
  - [28] Carle, S.F., Fogg, G.E.: Modeling spatial variability with one and multi-dimensional continuous-lag markov chains. *Mathematical Geology* **29**(7), 891–918 (1997)
  - [29] Strebelle, S.: Conditional simulation of complex geological structures using multiple-point statistics. *Mathematical geology* **34**(1), 1–21 (2002)
  - [30] Deutsch, C.V., Journel, A.G.: Gslib. Geostatistical software library and user’s guide **369** (1998)
  - [31] Carle, S.F.: T-progs: Transition probability geostatistical software. University of California, Davis, CA **84** (1999)
  - [32] Kolditz, O., Bauer, S., Bilke, L., Böttcher, N., Delfs, J.-O., Fischer, T., Görke, U.J., Kalbacher, T., Kosakowski, G., McDermott, C., *et al.*: Opegeosys: an open-source initiative for numerical simulation of thermo-hydro-mechanical/chemical (thm/c) processes in porous media. *Environmental Earth Sciences* **67**(2), 589–599 (2012)

- [33] Horgue, P., Soulaire, C., Franc, J., Guibert, R., Debenest, G.: An open-source toolbox for multiphase flow in porous media. *Computer Physics Communications* **187**, 217–226 (2015)
- [34] Flemisch, B., Darcis, M., Erbertseder, K., Faigle, B., Lauser, A., Mosthaf, K., Müthing, S., Nuske, P., Tatomir, A., Wolff, M., *et al.*: Dumux: Dune for multi-{phase, component, scale, physics,...} flow and transport in porous media. *Advances in Water Resources* **34**(9), 1102–1112 (2011)
- [35] Armstrong, M., Galli, A., Beucher, H., Loc'h, G., Renard, D., Doligez, B., Eschard, R., Geffroy, F.: *Plurigaussian Simulations in Geosciences*. Springer, ??? (2011)
- [36] Koltermann, C.E., Gorelick, S.M.: Heterogeneity in sedimentary deposits: A review of structure-imitating, process-imitating, and descriptive approaches. *Water Resources Research* **32**(9), 2617–2658 (1996)
- [37] Linde, N., Renard, P., Mukerji, T., Caers, J.: Geological realism in hydro-geological and geophysical inverse modeling: A review. *Advances in Water Resources* **86**, 86–101 (2015)
- [38] Mandelbrot, B.B., Van Ness, J.W.: Fractional brownian motions, fractional noises and applications. *SIAM review* **10**(4), 422–437 (1968)
- [39] Carle, S.F., Fogg, G.E.: Transition probability-based indicator geostatistics. *Mathematical geology* **28**(4), 453–476 (1996)
- [40] Weissmann, G.S., Carle, S.F., Fogg, G.E.: Three-dimensional hydrofacies modeling based on soil surveys and transition probability geostatistics. *Water Resources Research* **35**(6), 1761–1770 (1999)
- [41] Tartakovsky, D.M., Dentz, M.: Diffusion in porous media: phenomena and mechanisms. *Transport in Porous Media* **130**(1), 105–127 (2019)
- [42] Van Genuchten, M.T.: *Analytical Solutions of the One-dimensional Convective-dispersive Solute Transport Equation* vol. 1661. US Department of Agriculture, Agricultural Research Service, ??? (1982)
- [43] Berkowitz, B., Cortis, A., Dentz, M., Scher, H.: Modeling non-fickian transport in geological formations as a continuous time random walk. *Reviews of Geophysics* **44**(2) (2006)
- [44] Yu, C., Warrick, A., Conklin, M.: A moment method for analyzing breakthrough curves of step inputs. *Water Resources Research* **35**(11), 3567–3572 (1999)
- [45] Kreft, A., Zuber, A.: On the physical meaning of the dispersion equation

- and its solutions for different initial and boundary conditions. *Chemical Engineering Science* **33**(11), 1471–1480 (1978)
- [46] Comolli, A., Hakoun, V., Dentz, M.: Mechanisms, upscaling, and prediction of anomalous dispersion in heterogeneous porous media. *Water Resources Research* **55**(10), 8197–8222 (2019). <https://doi.org/10.1029/2019WR024919>
- [47] Sherman, T., Engdahl, N.B., Porta, G., Bolster, D.: A review of spatial markov models for predicting pre-asymptotic and anomalous transport in porous and fractured media. *Journal of Contaminant Hydrology* **236**, 103734 (2021)
- [48] Municchi, F., Icardi, M.: Generalized multirate models for conjugate transfer in heterogeneous materials. *Physical Review Research* **2**(1), 013041 (2020)